



Steininger, R., Barakos, G. N. and Woodgate, M. N. (2023) Numerical Analysis of HVAB and STAR Rotor Blades using HMB3. In: AIAA SCITECH 2023 Forum, National Harbor, MD, USA, 23-27 Jan 2023, ISBN 9781624106996.

This is the Author Accepted Manuscript.

There may be differences between this version and the published version. You are advised to consult the publisher's version if you wish to cite from it.

<http://eprints.gla.ac.uk/286153/>

Deposited on: 30 November 2022

Enlighten – Research publications by members of the University of Glasgow
<http://eprints.gla.ac.uk>

Numerical Analysis of HVAB and STAR Rotor Blades using HMB3.

Rinaldo Steininger^{*}, George N. Barakos[†] and Mark N. Woodgate[‡]
School of Engineering, University of Glasgow, Glasgow, United Kingdom, G12 8QQ

Computational Fluid Dynamics simulations of the Hover Validation and Acoustic Baseline, Smart Twisting Active Rotor, and Active Twist Rotor blades in hover are presented. For these blades, the effect of twist in hover is examined, using the in-house simulation tools of Glasgow University. Rigid and aeroelastic methods are also compared for these rotors. In forward flight, high-twist may be associated with increased blade vibration. For the Smart Twisting Active Rotor blades, the effect of static twist and of a 2/rev harmonic active twist input are also investigated at a high advance forward ratio flight conditions. A vibration index is used to quantify the harmonic components of hub forces and moments. The hover simulations were computed on grids of 10–16m cells, coupled with structural updates. The results show the strong effect of blade twist on hover performance. The forward flight cases were computed on a 36m cell grid and using a modal aeroelastic method.

I. Nomenclature

a_∞	=	free stream speed of sound, m/s
c	=	rotor blade chord, m
C_D	=	coefficient of drag, $L/(\pi\rho_\infty V_{tip}^2 R^2)$
C_L	=	coefficient of lift, $D/(\pi\rho_\infty V_{tip}^2 R^2)$
C_Q	=	coefficient of torque, $Q/(\pi\rho_\infty V_{tip}^2 R^3)$
$C_T = C_T^{US}$	=	coefficient of thrust, $T/(\pi\rho_\infty V_{tip}^2 R^2)$
D	=	rotor drag (wind axes backward), N
FM	=	figure of merit, $C_T^{3/2}/(2C_Q)$
L	=	rotor lift (wind axes upward), N
L/D_e	=	lift/drag-equivalent $\frac{C_L/\sigma}{C_D/\sigma + C_Q/\sigma/\mu}$
M_{tip}	=	tip Mach number V_{tip}/a_∞
N_B	=	number of rotor blades
Q	=	rotor torque, Nm
R	=	rotor blade radius, m
T	=	rotor thrust (shaft-axis upward), N
Q	=	rotor torque, Nm
V_{tip}	=	rotor tip speed, m/s ²
α_s	=	rotor shaft angle, degrees
β	=	blade root coning angle, degrees
θ_{75}	=	blade collective angle with reference to 75% of chord, degrees
μ	=	rotor advance ratio, V_∞/V_{tip}
ρ_∞	=	free stream density, kg/m ³
σ	=	rotor solidity, $\frac{R\pi}{N_B c}$
AFC	=	Active Fibre Composite
AIAA	=	American Institute of Aeronautics and Astronautics
ATR	=	Active Twisting Rotor
BERP	=	British Experimental Rotor Programme

^{*}PhD Student, CFD Laboratory, r.steininger.1@research.gla.ac.uk, AIAA Student Member.

[†]Professor, CFD Laboratory, george.barakos@glasgow.ac.uk, AIAA Senior Member.

[‡]Research Associate, CFD Laboratory, mark.woodgate@glasgow.ac.uk, AIAA Member

CFD	=	Computational Fluid Dynamics
CFL	=	Courant-Friedrichs-Lewy
CSD	=	Computational Solid Dynamics
FEM	=	Finite Element Method
HVAB	=	Hover Validation and Acoustic Baseline
HPW	=	(AIAA) Hover Prediction Workshop
MFC	=	Macro Fibre Composite
NASA	=	National Aeronautics and Space Administration
PSP	=	Pressure Sensitive Paint
RANS	=	Reynolds Averaged Navier-Stokes
SAS	=	Scale Adaptive Simulation
SST	=	Shear Stress Transport
STAR	=	Smart Twisting Active Rotor
URANS	=	Unsteady Reynolds Averaged Navier-Stokes
VI	=	Vibration Intrusion index

II. Introduction

The AIAA Hover Prediction Workshop (HPW), ongoing since 2014, is a collaborative effort to compare rotor hover prediction capabilities. The overview of its activities can be found on the official website[1], with sessions detailed from 2014 onward. Successful prediction workshops using experiments with the S-76[2] and PSP[3] rotors have been organised and contributions made with HMB2/HMB3 are briefly discussed here. The HPW sessions provide an overview of the numerical prediction work, with a large number of publications on the HVAB[4] rotor.

Previously, the HMB2/HMB3 CFD/CSD tool set of the University of Glasgow was used to contribute hover predictions. Jimenez-Garcia and Barakos[5] closely matched the experimental figure of merit on the hovering S-76 rotor using meshes of 9 and 30 million cells. An analysis on the S-76 CFD results and comparison with the HPW experiment is given in [6]. In another work on the XV-15 and the ERICA tilt rotors[5, 7], the XV-15 hover prediction[8] compared the fully turbulent $k - \omega$ SST and the $k - \omega$ SST- γ transition models at Reynolds number of 5 million. That work also included initial results on the HPW PSP (Pressure Sensitive Paint) rotor and was extended with a comparison between a second order and a fourth order muscle extrapolated scheme in [9]. The XV-15 rotor is a three-bladed design, with highly twisted (-40.25 degrees/R), almost rectangular planform, of solidity 0.089. The rotor radius is 3.81 m. The S-76 rotor is a four-bladed, swept and tapered rotor with 1.432 m radius, and solidity of 0.07, giving it a similar aspect ratio to the STAR[10–12] rotor. The linear twist rate is 10 degrees/R, where R is the rotor radius. The taper and sweep closely match the HVAB blade tip. The PSP rotor results in hover matched the experimental results as published by Jimenez-Garcia and Barakos[13] and Fitzgibbon *et al.* [14], with the latter work comparing fixed and free transition results, and explaining in more detail the PSP blade results in level flight. The PSP rotor is very close to the HVAB planform, described in Section IV. The geometric differences are confined to trailing edge, and the blade sweep break. The hover wake breakdown on the PSP rotor was shown in HMB3 and an 158 million cell grid, with URANS and SAS[15]. The loads were closely matched with RANS simulations and the vortex wandering was clearly observed in the SAS solution. Through all the aforementioned works, HMB3 could successfully predict the hover figure of merit within 1 count with the correct settings applied for the problem. The thrust and torque and radial loading distributions correlated well with experiments. For RANS and URANS results in hover using HMB3, meshes of the order of 5m cells per blade and 7m per periodic section in the background were sufficient for accurate hover simulations, and this practice was followed in this work too.

This work focuses on the importance of blade twist in hover and forward flight. Therefore, the HVAB, STAR and ATR rotor blades are compared in hover with nominal and increased twist. The STAR and ATR rotors were chosen as they both feature blade integrated torsion actuators. All rotor blades in this work have simple rotor blade tips, either cut-off straight or with a small sweep-taper. The HVAB rotor tips also have reduced thickness, but a trailing edge tab, scaled to full size. Non-planar, complex rotor blades and advanced tips as seen on the Blue Edge[16] rotor or the BERP[17] (British Experimental Rotor Programme) rotors are not considered here, to isolate the effect of twist.

For a hovering rotor, the main contribution to its power is induction, which means, based on momentum theory, that the rotor disk area should be maximised to reduce the induced velocity. Theory predicts that the most efficient hovering rotor is one, which has a uniform downwash velocity over the whole rotor disk. This can be approximately achieved with the 1/R blade twist distribution. Therefore, higher blade twist, within reason, for helicopter main rotors will always

lead to greater hover efficiency. It is also believed that high twist is a disadvantage in forward flight. Therefore, the STAR rotor with nominal and higher twist is also simulated in high-speed forward flight. The STAR rotor[10–12] is equipped with piezoceramic twist actuators which allow static and dynamic twist change. In literature, 2/rev dynamic blade pitch, twist or actuation through trailing edge flaps showed large power and vibration benefits with lower fidelity methods, and a small benefit in experiments and high-fidelity methods. The ATR uses a similar skin embedded actuator type, but has been tested in heavy gas. All three rotor blades are of simple planforms, allowing for the effect of blade twist to be isolated from other design features like blade tip anhedral, or advanced blade tip designs. The nominal and increased twist hover simulations cover distributions from 8 to 18 degrees/R.

III. HMB3 CFD/CSD framework

All simulations were computed using the Helicopter Multi-Block 3 in-house software tool[18]. It is a finite volume solver and overset grids were used. HMB3 solves the Unsteady Reynolds Averaged Navier-Stokes (URANS) equations in integral form using the Arbitrary Lagrangian Eulerian (ALE) formulation for time-dependant domains, including moving boundaries. To evaluate the convective fluxes, the Osher[19] approximate Riemann solver is used, while the viscous terms are discretised using second order central differences. The MUSCL approach of Leer[20], is used to provide high-order accuracy in space with the alternative form of the Albada limiter[21] in regions of large gradients. Implicit, dual-time stepping method of Jameson[22] is employed. The linearised system of equations is solved using the Generalised Conjugate Gradient method with a BILU factorisation as a pre-conditioner[23]. One- to four-equation turbulence models are available in HMB3. The 1994 $k-\omega$ SST model of Menter[24] is used for the computations presented in this paper.

The hover out of ground effect (OGE) simulations in HMB3 use the Froude boundary condition. A rotational quarter of the rotor domain is simulated with periodic boundary conditions, when using the steady formulation. The rotational velocity component is accounted for by a source term in the ALE discretised Navier-Stokes equations as seen in Equation 1. The hovering rotor grids are cylindrical domains with their velocity adjusted to account for the rotor induction. The hover boundary conditions are shown in Figure 4 (b). The semi-discrete equations are:

$$\frac{d}{dt} \int_{V(T)} \mathbf{W} dV + \int_{\partial V(T)} (\mathbf{F}^i(\mathbf{W}) - \mathbf{F}^v(\mathbf{W})) \mathbf{n} dS = S. \quad (1)$$

The aeroelastic calculations in hover with HMB3, are using MSC NASTRAN and weak coupling. The aeroelastic model for the forward flight is modal. Assuming the blade shape ϕ is a sum of the modes ϕ_i , representing the blade displacements for each mode, multiplied by the coefficients α_i :

$$\phi = \phi_0 + \sum_{i=1}^{n_m} \alpha_i \phi_i, \quad (2)$$

where ϕ_0 is the undeformed shape. The problem is then reduced to solving for the coefficients α_i . By projecting the FE equations of motion of an elastic structure onto the mode shapes and assuming that the mode shapes have been scaled to give dimensional generalised masses $m_i = 1$, the modal equations of motion are:

$$\frac{\partial^2 \alpha_i}{\partial t^2} + 2\zeta_i \omega_i \frac{\partial \alpha_i}{\partial t} + \omega_i^2 \alpha_i = \mathbf{f} \cdot \phi_i, \quad (3)$$

where \mathbf{f} are the aerodynamic forces of the blade projected on each structural grid point, ω_i is the eigenpulsation and ζ_i is the structural damping coefficient[25].

IV. Rotor Geometries

While the HVAB rotor is designed with a swept-tapered rotor tip and multiple aerofoils over the span, the STAR and ATR rotor blades are rectangular planform, single aerofoil designs. The main properties of the rotors are compared in Table 1. The rotor size and planform are illustrated in Figure 1. Due to the low dynamic head near at the blade root in hover, the STAR blade root section was only included in the rotor mesh of the level flight case. For each blade, the hover simulations are done for the nominal twist, and for a similar blade with 4 degrees/R increased linear twist rate. The twist levels of each individual blade are shown in Figure 2, where the solid lines represent baseline blades, and dash dotted represent the increased twist models.

Table 1 Rotor properties.

Name	Radius [m]	Chord [m]	N_B	Solidity	Twist [$^\circ$ /R]	M_{tip}	V_{tip} [m/s]	Aerofoils
HVAB	1.689	0.138	4	0.104	-14	0.65	221.2	RC(4), RC(6)
STAR	2.000	0.121	4	0.077	-8	0.641	218.0	NACA23012
ATR	1.397	0.108	4	0.098	-10	0.60	100.7	NACA0012

The AIAA Hover Validation and Acoustics Baseline (HVAB) rotor is used to compare the current numerical prediction capabilities of hovering rotors. It is geometrically similar to the PSP rotor, but has a thicker trailing edge and differs in weight and structural properties. The rotational speed is 1250 RPM (131 rad/s). The rotor blade uses RC-series helicopter aerofoils, which are blended as seen in Figure 1. The latter part of the aerofoil name designates the thickness in % of chord length. All aerofoils were modified to have a uniform trailing edge thickness of 0.035 in [4]. The rotor blade has a high linear twist rate of -14 degrees/R with zero pitch defined at 75% R. The rotor blade radius is 66.50 in, with a cutout at 14% R, the root fairing blends into the blade section at 25.19% R, and the main section chord is 5.45 in, before it tapers to 3.27 in. The 30 degrees swept leading edge at the tip intersects the main leading edge at 95% R, however the transition is rounded off at the leading edge with a 0.5 in sweep break.

The Smart Twisting Active Rotor (STAR) is based on a scaled Bo-105 rotor. It features a nominal twist rate of -8 degrees/R, a chord length of 12.1 cm and a radius of 2 m from the shaft axis as seen in Figure 1. The nominal speed is 1041 RPM (109 rad/s). The blade is of constant chord, rectangular planform, with the reference pitch axis at the quarter chord. The aerofoil for the STAR rotor is a modified NACA 23012 section with a flat trailing edge, 1.0 mm thick and 5.4 mm long. The tip speed of this rotor is 218 m/s. The macro fibre-composites (MFC) used in the construction of the blades allow a static twist deflection of up to 4 degrees peak-to-peak[12] (3 degrees pitch up, 1 degree pitch down).

The ATR is a 4-bladed rotor, designed for heavy gas (R-134a). At the pressure and temperature of the ATR experiments, the ratio of specific heats γ is 1.116 and the speed of sound is 167.8 m/s. The rotor speed is 688 RPM (72 rad/s). This rectangular planform uses a NACA0012 section over the whole length of the blade, and the structural properties available in the literature are reported uniform along the span. The rotor has active-fibre composite (AFC) actuators embedded, which could be used to achieve up to 1.1 degrees of peak-to-peak static twist change (± 0.55 degrees).

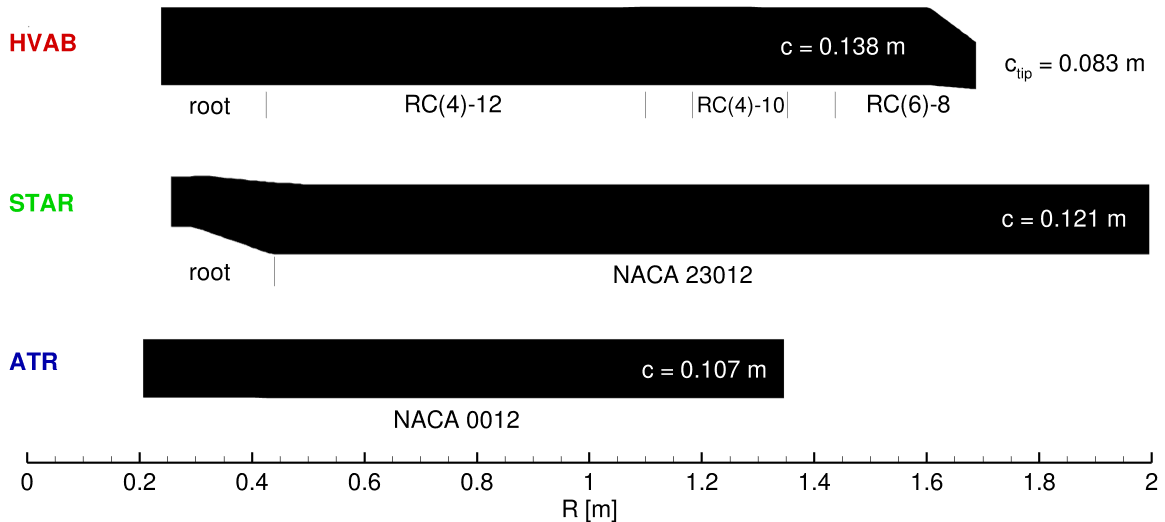


Fig. 1 Planforms of the three rotor blades examined. The STAR rotor is mirrored to show clockwise rotation direction.

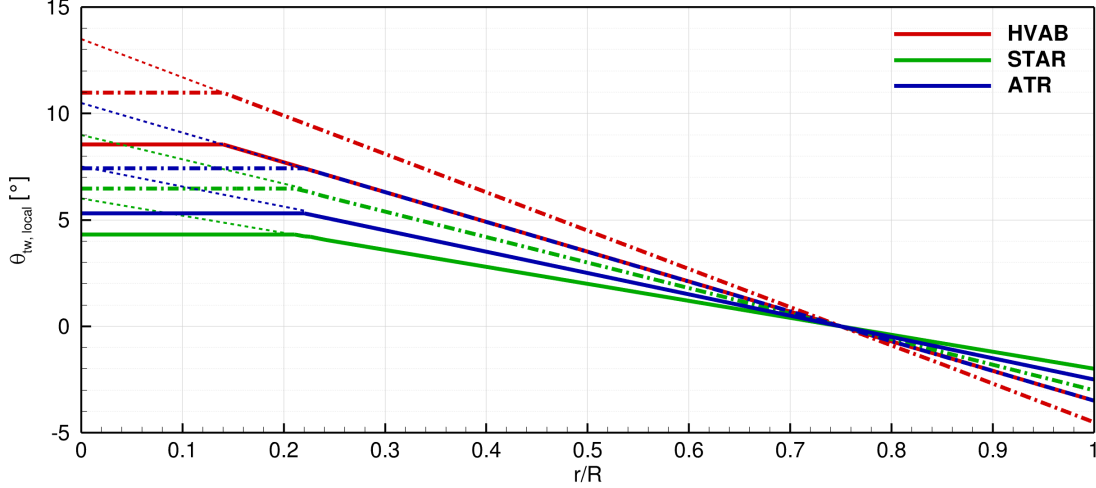


Fig. 2 Blade twist distribution of the three rotor blades. Dash-dotted line shows the corresponding blade with an linear twist rate increase of 4 degrees/R and dotted thin lines as root extrapolation.

Table 2 Rotor blade meshes number of cells and spacing.

Name	chordwise	normal	spanwise	background spacing
HVAB	142	64	148	5%c
STAR	154	68	210	5%c
ATR	154	45	176	5%c
STAR FF	142	64	220	15%c

V. Rotor CFD Grids

The employed CFD grids have been generated using Ansys ICEM CFD Hexa. An overset grid method was used to split the domain into a background and a blade mesh. A C-H topology was chosen for the all three blades, overhanging on both spanwise ends of the blade to capture the tip and root effects. The hover blades are modelled with a first layer height of $10^{-5}c$, which corresponds to a $y^+ \approx 1$. A hyperbolic distribution of nodes with an expansion ratio below 1.20 at all surface normal directions was chosen to allow sufficient resolution in the viscous buffer layer. The outmost layer of the chimera boundaries on the foreground blade grids is sized to 0.08 chords on the STAR rotor, and 0.05 chords on the HVAB rotor. 5% chord foreground and background grids were aimed for in the region near 20% R inboard and outboard of the blade tip, and the refinement was extended along the tip vortex path for at least three vortex ages. The blade root spacing was coarsened to facilitate faster turnaround times. The surface normal blocks on the HVAB blade grid were split to include a 40 cell wide block layer in the boundary layer region of 1% chord thickness to produce good near-surface cells. The point distributions for the hover blades are shown in Figure 3. Convergence speed-ups were observed until CFL number 20 for hover.

The blade background-grid is similar for all hover, cases, but with some changed number of grid points to keep the mesh near 5% of chord in the near grid region. The boundary conditions and cell distribution is shown in Figure 4. The circumferential spacing at the blade tip radius is slightly larger, at 8% of chord. An effort was made, to match the blade and background grid spacings, and an inverse distance weighted approach was used for the chimera interpolation.

The background grid for the rotor forward flights is shown in Figure 5. A three-level chimera method is used, with free stream in/outflow conditions on the domain boundary. The rotor shaft angle is simulated via the free stream inflow. The domain is a cylinder of 30 radii in diameter around the centre of rotation. The near blade background grid is a cylindrical disk, of which a quarter is shown in Figure 5 (b). This disk is rotating with the rotor blades. A small flattened sphere sits at the centre to generate some disturbance of the hub. The disk is made of 11.4 million cells, which brings the full forward flight grid to 36.5m cells. In the region of the rotor blade tips, the disk spacing is 5% of chord and the radial resolution is 0.55 degrees per cell. The radius of the disk is 1.3 times the rotor blade radius.

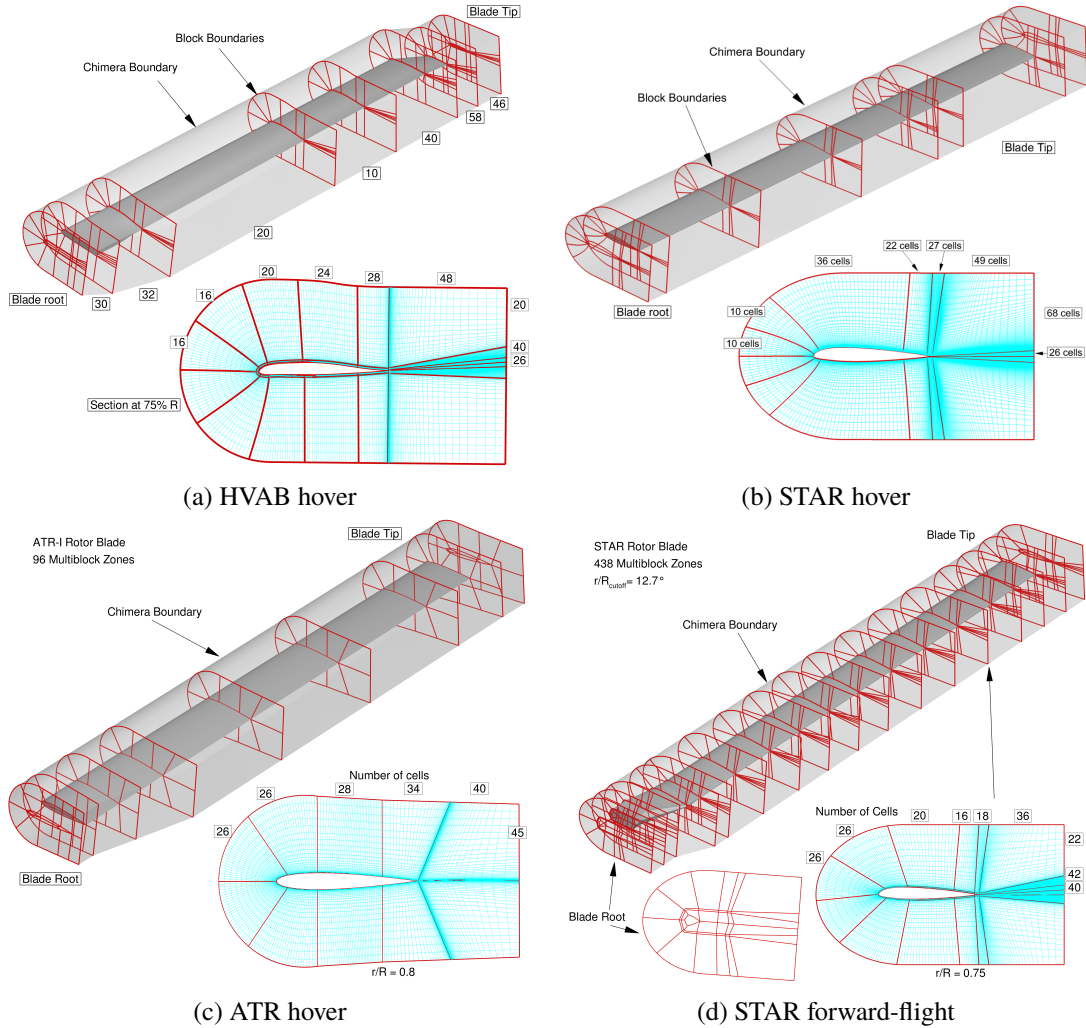


Fig. 3 HVAB hover blade mesh blocking structure and cell distributions for HVAB hover (5.35m cells), STAR hover (5.35m cells), ATR hover (3.06m cells) and STAR FF (5.13m). Boxes indicate Number of cells per edge.

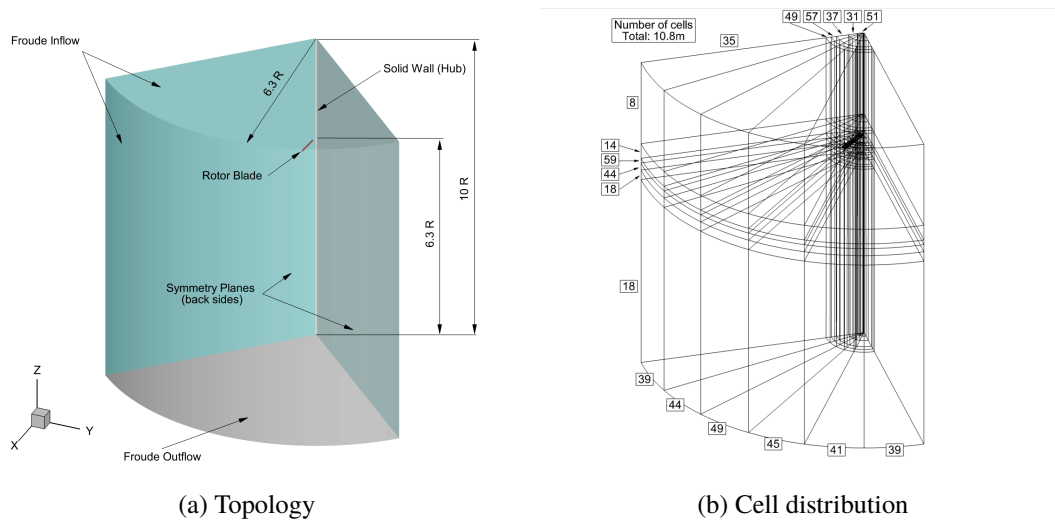


Fig. 4 Hover background topology, boundary conditions and cell distribution for the 10.8m cell background

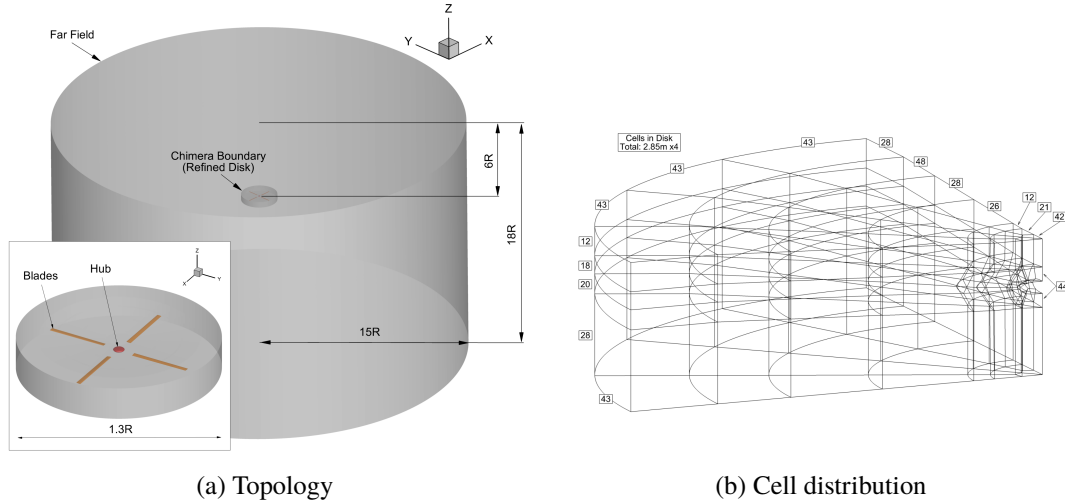


Fig. 5 STAR forward flight CFD grid, boundary conditions and cell distribution.

VI. Dynamic Modelling of Rotor Blades

For all rotor blades, beam models have been created as input files to MSC NASTRAN. Deformations could be directly extracted for steady cases, and in forward flight, the structural mode shapes, amplitudes and frequencies were obtained and used as input files for HMB3. The MSC NASTRAN elements of the HVAB rotor 1D-beam model are shown in Figure 6. All rotors in this work are considered rigid inboard of the lag-flap hinge. The FEM grid points for the beam elements were all defined on the quarter chord location, which is a straight line from the centre of rotation. For each point, two additional FEM points have been defined ahead of the leading edge and behind the trailing edge. Between these outer points, rigid bar elements were inserted. These elements have no mass or other structural properties and are only used to interpolate the resultant forces from the CFD grid onto the structure. The NASTRAN CBEAM elements include the properties of area, moment of inertia in flap and lag, torsional stiffness, mass/length and the locations of the centre of gravity and neutral axis and the pre-twist angle. All sectional properties were converted to the metric kg-N-m-s system.

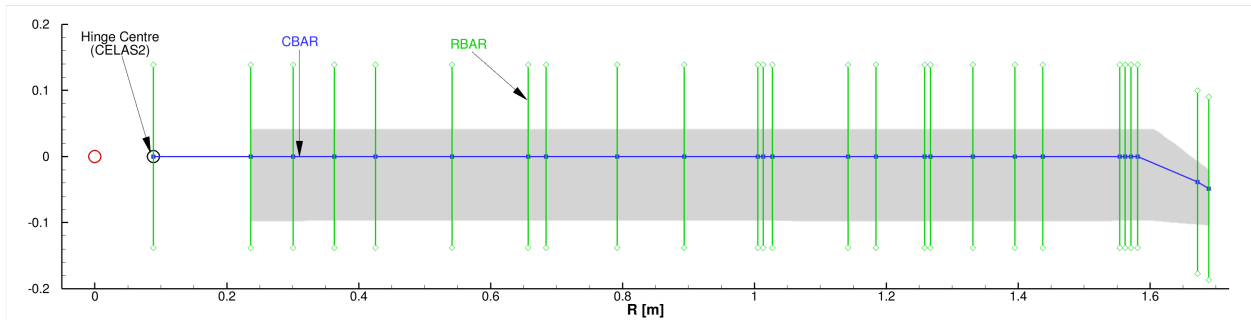


Fig. 6 HVAB rotor blade beam model. The centre of rotation is at (0,0). The blue sections between the green bars represent the cross-sectional beam elements (CBEAMS). The Rigid Bars (RBARS), which are used to interpolate aerodynamic loads onto the structure are shown as green.

The numerically obtained, cross-sectional properties for the HVAB rotor were provided in [4]. A correction to the given units is published on the AIAA Hover Prediction Workshop webpage[1]. The model in this work uses the properties for the blades SN001–005. Values from $r/R = 0.178$ (0.3 m) to $r/R = 0.98$ were provided, and any points inboard were considered rigid. Instead of a modelled hinge, the pre-coning angles have been applied, which reduces the required number of updates on the structural deformations.

The 1D-beam model of the STAR rotor is shown in Figure 7. The flap-lag hinges at the radial position of $0.0375 R$ are fully modelled in the beam. The hinges are in flap, lag, pitch order. It comes with a lag-spring damper with a

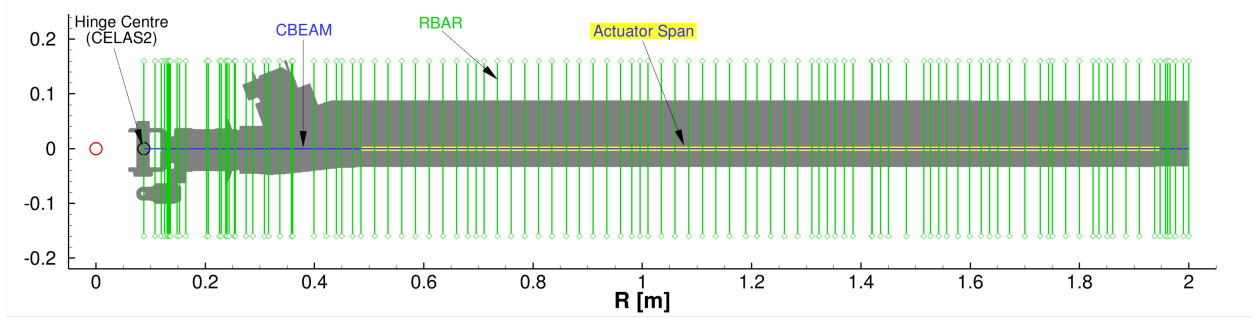


Fig. 7 STAR rotor blade beam model. The centre of rotation is at (0,0). The blue sections between the green bars represent the cross-sectional beam elements (CBEAMs). The yellow underlining of the beams represents the spanwise sections, which include the active twist composites. The Rigid Bars (RBARs), which are used to interpolate aerodynamic loads onto the structure are shown as green. The silhouette of the full rotor blade is in the background.

Table 3 Blade Eigenfrequencies for HVAB at 1250 RPM and STAR at 1041 RPM.

HVAB		STAR	
Mode	Frequency [Hz]	Mode	Frequency [Hz]
Lag 0 (hinge)	∞ (rigid)	Lag 0 (hinge)	6.69
Flap 0 (hinge)	∞ (rigid)	Flap 0 (hinge)	18.0
Flap 1	26.3	Flap 1	42.0
Flap 2	32.9	Torsion 1	62.9
Lag 1	68.2	Flap 2	70.1
Torsion 1	122	Lag 1	101
Flap 3	167	Flap 3	117

stiffness of roughly 3013 Nm/rad. The damping is applied within HMB3. Additionally, a flap spring with small stiffness (10 Nm/rad) is required for the NASTRAN model's rigid flapping mode to converge a steady solution. The structural properties of the STAR blades and hinges have been provided as part of the STAR prediction effort. The cross-sectional parameters for the ATR-I blade were available between $r/R=0.3$ to $r/R=0.97$, when they were obtained from Shin[26]. The corresponding regions contains the piezoelectric AFC actuators. All available literature gives constant properties along this span. For the analysis in this section, these parameters were used from the hinge centre until the blade tip, because no information, except exterior images, were available for the root section. Inboard the hinge centre, the rotor is considered rigid. A pitch spring of 100 Nm/rad and a lag spring of 5 Nm/rad were included to converge the rigid lag and flap modes, since no pre-cone angles were given.

The eigenfrequencies of the HVAB and STAR rotors are shown in Table 3. The HVAB rotor with the rigidly modelled hinge, does not have hinge modes. The first torsional mode eigenfrequency of the STAR blade is close to the Blade Passing Frequency (BPF) and designed to increase active twist control authority for 3/rev and 4/rev. The first torsional eigenmode and the third flapping mode are coupled and are neither pure torsional or flapping. The third torsion and fifth flapping mode also show such behaviour. The eigenfrequency of the first 8 modes, including rigid lag and flap, were compared with results of Shin *et al.* [26]. The values at nominal RPM are compared in Table 4. The first five modes show good frequency correlation, however the third flapping shows a larger difference.

VII. Results and Discussion

The test conditions of the hover tests in this abstract are summarised in Table 5. All force and moment coefficients use the US definition, as shown in the nomenclature. The HVAB rotor was simulated using the predicted cone and lag angles, which were based on results of the PSP rotor and updated with the HVAB properties by the HPW. In the aeroelastic simulation case, the hinges were fixed at the prescribed values, with the blade allowed to deform outboard.

Table 4 ATR-I blade Eigenfrequencies at 688 RPM.

Mode	Frequ. UofG [Hz]	Frequ. Shin[26] [Hz]	Difference [%]
Lag 0 (hinge)	4.03	3.70	8.92
Flap 0 (hinge)	11.9	11.9	0.00
Flap 1	31.7	30.8	2.92
Flap 2	56.5	53.8	5.02
Lag 1	60.3	60.9	-0.99
Torsion 1	64.7	67.2	-3.72
Flap 3	103	88.8	15.99

Table 5 Hover test conditions presented.

Blade	Twist θ_{tw} [degrees]	Elastic	Collective θ_{75} [degrees]	Root Coning β [degrees]
HVAB	-14	no	6, 8, 10	0.4, 0.8, 1.3
HVAB	-18	no	6, 8, 10	0.4, 0.8, 1.3
HVAB	-14	yes	6, 8, 10	0.4, 0.8, 1.3
HVAB	-18	yes	10	1.3
STAR	-8	no	5, 7, 9, 11, 12	2.5, 2.5, 2.5, 2.5, 2.5,
STAR	-12	no	5, 7, 9, 11, 12	2.5, 2.5, 2.5, 2.5, 2.5,
STAR	-8	yes	6.8, 8.4, 9.9, 10.6, 11.6	0.0 0.0 0.0 0.0 0.0
STAR	-12	yes	9.9	0.0
ATR	-10	no	10	1.0
ATR	-14	no	10	1.0

For the STAR and ATR rotors, the blade hinges for the rigid blade simulations were prescribed. In the aeroelastic STAR hover simulation, the blades were freely hinged and flapped until steady state positions were found. This, however, substantially increased the time for the blade loads and deformations to settle down and required some underrelaxation. Simulations were considered converged, when the loads reached a plateau, with residual values in HMB3 dropping 8 to 9 orders of magnitudes. Steady simulations converged after 40000 iterations, but were left to run beyond 100000. The aerodynamic loads have been averaged over iterations where a quasi-steady state has been reached. Structural updates were applied every 15000 to 20000 steady iterations, depending on the convergence of the loads. The STAR elastic cases required roughly 10 deformation updates to reach a converged state out of an oscillatory behaviour, the HVAB required at least five.

A. HVAB Blade in Hover

The figure of merit curve and the thrust produced for each simulated pitch angle is shown in Figure 8 (a). A peak figure of merit of 0.71 was predicted on the rigid HVAB rotor with the fully turbulent boundary layer model. The elastic blade indicates a slightly higher hover efficiency. The figure of merit is slightly under predicted when compared to the expected results of the wind-tunnel, because the laminar flow regions, specially on the pressure side, are not represented in the turbulence model. The elastic blade produces less thrust for a given root collective angle due to the elastic pitch down deformation over the blade span. The thrust coefficients are shown in Figure 8 (b). The blade, which was rigidly deformed to -18 degrees/R in twist, showed the highest figure of merit, increasing the nominal twist FM by two counts. Similarly, the higher twisted blade achieved a 2 count improvement over the baseline elastic blade at 10 degree pitch angle. The additional pitch down deformation on the aeroelastic simulation of the high-twist HVAB blade, indicates a small further improvement in hover efficiency.

In Figure 9, the sectional thrust coefficients show loading peaks at 94% of the radius. The location is unchanged for the elastic and high-twist cases, but shifts slightly outboard at lower thrust. This is expected due to the lower tip vortex convection at lower pitch, as the thrust peak is a product of the induced velocity from the previous vortex passage. A dip

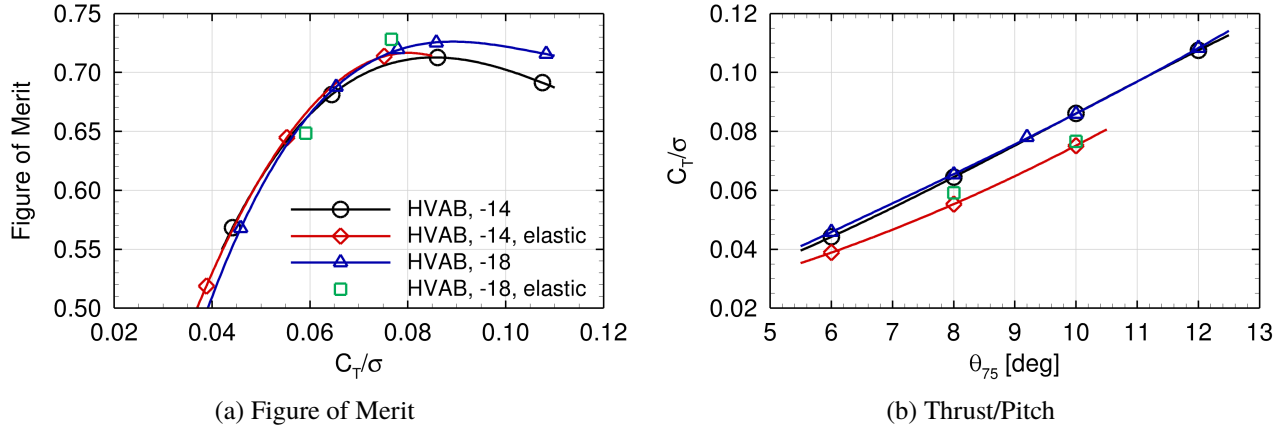


Fig. 8 Figure of Merit over thrust coefficient and thrust coefficient at blade pitch of the HVAB rotor blade.

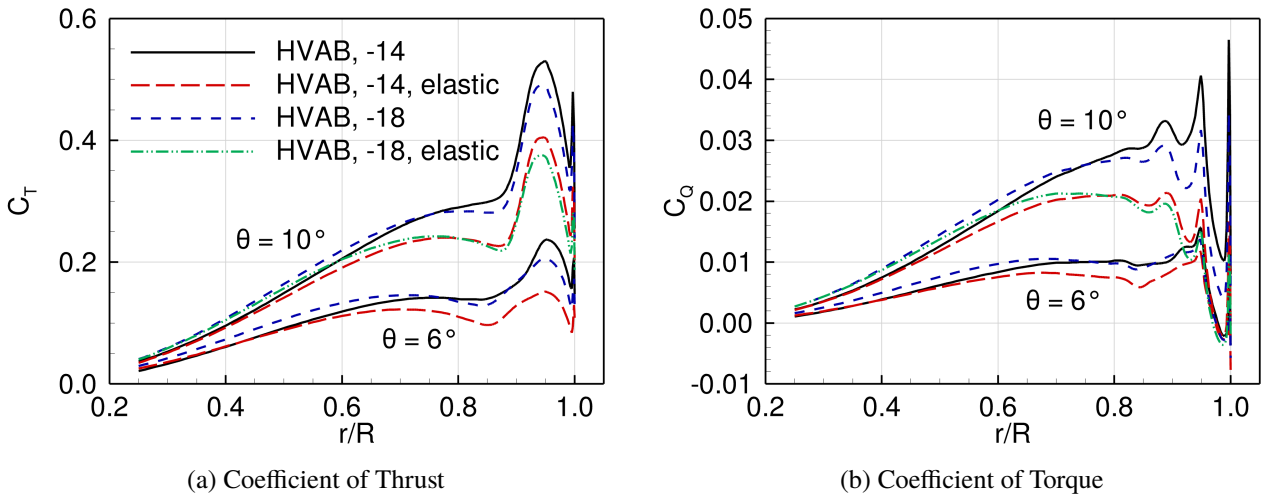


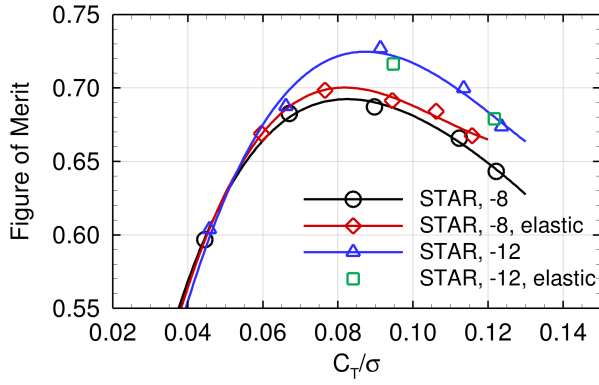
Fig. 9 Coefficients of thrust and torque for selected collective angles of the HVAB rotor blade (pressure only).

in sectional thrust is observed inboard of the peak thrust. This is a product of the reduced tip vortex strength in the cases with tip down torsional deflection. This is specially pronounced in the low pitch setting. The effect of the tip vortex growth can be seen outboard, where the tip relief causes a spike in sectional thrust. The high twist cases are expected to produce a similar thrust when compared to the nominal blades, with more loading inboard of 75%R, but less outboard. The sectional torque coefficient peaks at 87.5% R, just inboard of the thrust plateau at the high pitch condition, before both cases show a peak torque at the location of peak sectional thrust. The torque then sharply falls toward the rotor tip, with a further peak at the tip vortex formation.

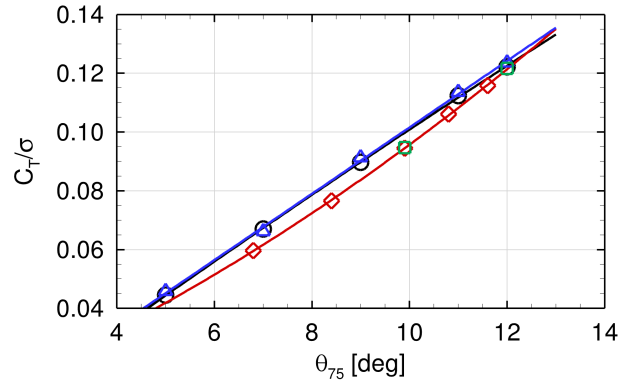
B. STAR Blade in Hover

The nominal STAR rotor blade, shows a peak figure of merit at just below 0.7 from the results of HMB3, shown in Figure 10 (a). The rigid rotor blade, compared with the elastic one, has a slightly lower figure of merit, as it lacks the elastic tip twist down, which effectively increases twist and also affects the stall characteristic at high thrust. The mesh with increased twist achieves a 4-count improvement in FM over the baseline, which equates to 1 count per degree of twist change. The aeroelastic blade showed 3 counts FM improvement. The elastic high twist blade, performed worse than the corresponding rigid blade. The blade thrust is marginally reduced due to the elastic deformations. At high pitch angles, however, the higher twisted blade produces more thrust than the baseline blade, as the rigid blade approaches a localised stall due to the thick aerofoil section and the effect of the tip vortex.

The distribution of the sectional thrust and torque components for two pitch angle settings are compared in Figure 11.

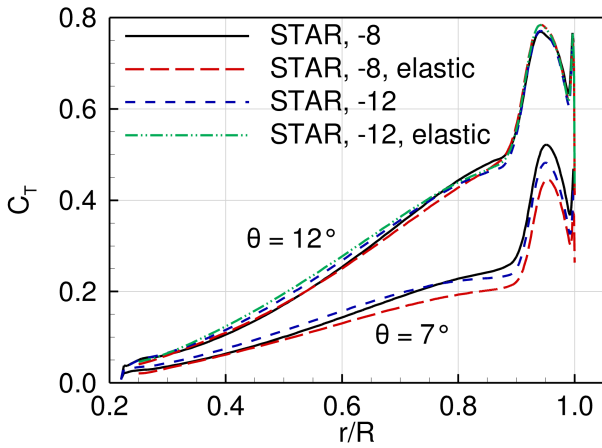


(a) Figure of Merit

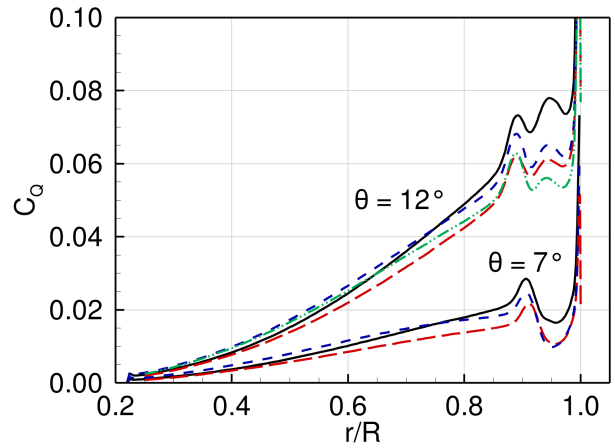


(b) Thrust/Pitch

Fig. 10 Figure of Merit over thrust coefficient and thrust coefficient at blade pitch of the STAR rotor blade.

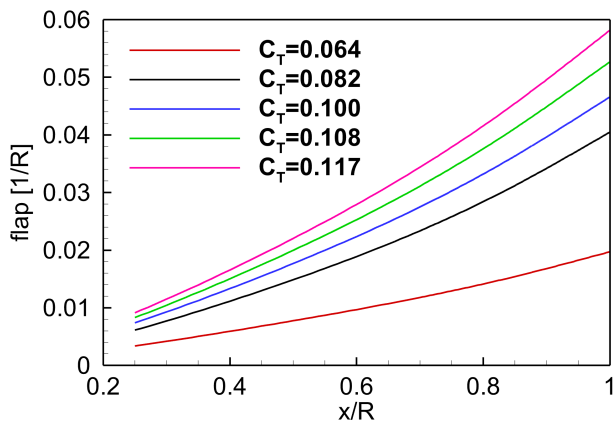


(a) Coefficient of Thrust

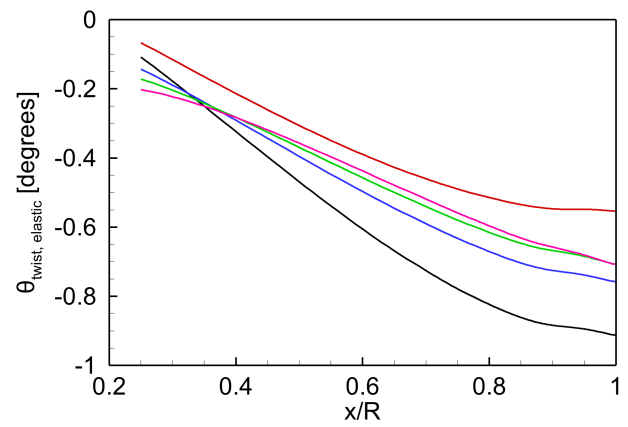


(b) Coefficient of Torque

Fig. 11 Coefficients of thrust and torque for selected collective angles of the STAR rotor blade (pressure only).



(a) Figure of Merit



(b) Thrust/Pitch

Fig. 12 STAR rotor blade deformations plotted over radius.

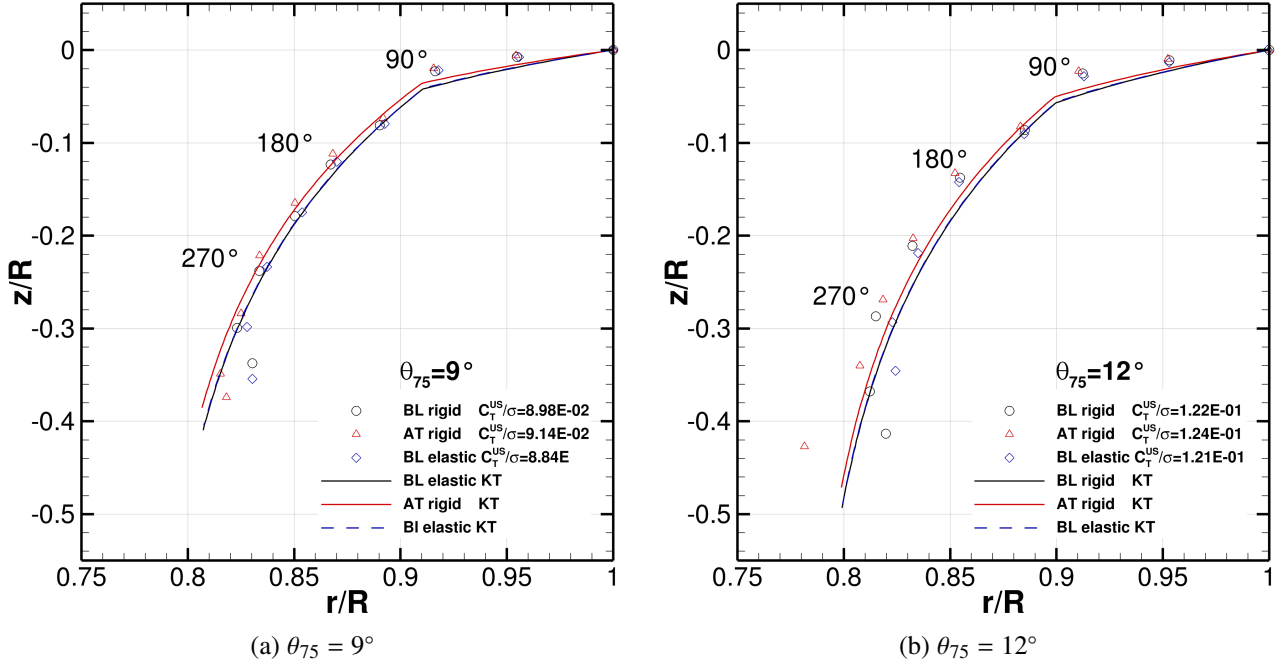


Fig. 13 Tip vortex convection of the hovering STAR rotor compared with the fit of Kocurek and Tangler (KT)[27].

Comparing the higher twist $\theta_{tw} = -12$ degrees/R rigid case against the baseline $\theta_{tw} = -8$ degrees/R, a clear trend of increased thrust on the inboard sections of the rotor blade can be observed. For all investigated pitch angles, the cross-over point is at 75% R, where the nominal blade twist is zero. The torque due to the drag force also increases in this section. In the outboard section, the blade is highly loaded. A characteristic peak forms for the thrust coefficient, where the higher twist blade shows the peak slightly further inboard, but noticeably lower for 7 degrees of collective pitch. At the high thrust setting, the outboard section produces a reduced lift on the higher twisted blade only where it is loaded less, but achieves the same peak thrust. This indicates, that the thick blade section is pitched too high outboard and experiences a thrust plateau due to onset of flow separation. The elastic blade thrust coefficient lies between the two rigid cases in the outboard section. At 11 degrees the peak thrust coefficient is 0.874 for the rigid baseline case, but 0.876 for the rigid, high twist case. The inboard torque coefficient is similar for both rigid and elastic baseline cases, while the higher local pitch of the high-twist case produces more drag. After 75% R the trend flips again, with a very significant torque reduction on the high-twist blade. At 11 degrees collective, a second torque peak forms at 95% R due to the increasingly transonic flow with peak Mach number of 1.4.

The aeroelastic deformations in hover for the STAR blade are shown in Figure 12. For all, but the lowest thrust setting, a linear increase in blade flap can be observed, reaching a peak value of 6% of radius at the blade tip on the highest thrust case. Due to the loading distribution, the blade is curved up outboard. The magnitudes of elastic blade twist were expected to be in order of the blade collective settings. However, the lowest thrust produces the lowest aeroelastic twist response, with a 0.5 degrees tip pitch down, while the second lowest thrust shows the largest deformation. With increasing thrust, the torsion settles around 0.7 degrees. It can be noted, that the blade overall produces a pitch down moment. The tip vortex of the first blade passage also has a visible effect on the torsion, and this effect is reduced at high thrust due to the increased downwash. The rotor also experiences an onset of stall due to the passage of the previous vortex at high thrust, which adds to the tip pitch down moment.

The tip vortex centre location was identified from the simulation results by finding the peak in vorticity magnitude at intervals of 45 degrees of vortex age. The results are compared to the empirical model of Kocurek and Tangler [27] in Figure 13. At low pitch settings and for the higher-twist blade, the tip vortex initially rises slightly above the following blade before pushed downward. At medium thrust settings, the tip vortex locations of the simulation match the model very well. The higher twist case is observed to have less downward convection than the baseline, as the model predicts. The aeroelastic results (BL, elastic) are very close to the rigid baseline data, but with the vortex being further up and

Table 6 ATR rotor hover results.

Twist [degrees/R]	C_T/σ	C_Q/σ	FM
-10	7.167×10^{-2}	6.792×10^{-3}	0.642
-14	7.228×10^{-2}	6.659×10^{-3}	0.663

inboard for a given vortex age. At the high thrust settings $\theta_{75} = 11$ and 12 degrees, the results match similarly, but more scatter in the solution is observed around one revolution of vortex age, as the vortex reaches a less refined area of the background mesh.

C. ATR Blade in Hover

The ATR rotor was tested at 10 degrees of pitch angle for rigid blades of nominal and increased twist. The figure of merit obtained for the baseline blade was 0.64, with the 4 degrees/R increased twist improving the figure of merit by another 2 counts. Rotor thrust and torque are shown in Table 6.

VIII. Effect of Twist in Forward Flight

The results of six different conditions of a level flight at high advance ratio $\mu = 0.349$ are shown in Tables 7 and 8. The cases labeled baseline, use the STAR rotor without any input to the simulated piezoceramic actuators. The high-twist cases use a 12 degrees/R STAR rotor blade, using the same twist increase over baseline in hover. Active twist cases use a harmonic input of 2/rev at a phase angle of 210 degrees. This phase corresponds to a peak pitch up at azimuth stations of 105 and 295 degrees. The peak-to-peak amplitude of the active twist is 2 degrees for this case, with a 0.5 degrees pitch-up offset. The high-twist cases use a 12 degrees/R STAR rotor blade, using the same twist increase over baseline in hover. The rotor was trimmed to a cruise flight condition at medium thrust and -11.11 degrees shaft tilt. The lift-to-drag equivalent ratio L/D_e of the tables equates the torque to the rotor propulsive force by the following equation: $L/D_e = \frac{C_L/\sigma}{C_D/\sigma + C_Q/\sigma/\mu}$. The vibration index (VI) is calculated from 4/rev and 8/rev harmonic components of force $F_{x,i}$, $F_{y,i}$, $F_{z,i}$ and roll, pitching moments $M_{x,i}$, $M_{y,i}$. Here, i represents the harmonic:

$$VI = \sum_{i=4,8} \left[\frac{\sqrt{(0.5F_{x,i})^2 + (0.67F_{y,i})^2 + (F_{z,i})^2}}{W_0} + \frac{\sqrt{(M_{y,i})^2 + (M_{z,i})^2}}{RW_0} \right], \quad (4)$$

where $W_0 = 3600$ N represents the nominal model scale weight and $R = 2$ m is the rotor radius. The same index is also described in reference [12].

Clear trends emerge comparing rigid and elastic computations, and between baseline, high twist and dynamically twisted rotor results. The inclusion of aeroelastics, required a collective pitch increase of 0.4 to 0.5 degrees, and an increase in cyclic inputs. The average tip pitch-down deformation in the elastic baseline case was 1.5 degrees. The harmonic twist application is predicted to reduce the required collective angle by roughly 1 degree in this case, as advancing and retreating side can be loaded more. The lateral cyclic is much higher in the rigid, active twist case than in the elastic, active twist case, due to the strong pitch down elastic deformation on the rotor advancing side. Overall, the rotor torque was higher on the rigid rotor simulations than with elastic blades, resulting in a lower lift to drag-equivalent ratio. For both rigid and elastic cases, the higher twist blades had the lowest efficiency, but this was less pronounced for the elastic blade. The rigid high-twist case shows an almost threefold increase in the vibration metric, for the elastic effect, the increase is small. The 2/rev harmonic twist managed to effectively reduce the vibration index over the baseline. The L/D_e was lower in the rigid simulation, but this could be recovered in the elastic blade case.

In the Mach-squared plots, the STAR rotor is shown as clockwise spinning with the free stream inflow from the left of the plot. The forces are in the blade frame of reference, with $M^2 C_n$ being upwards normal of the airfoil section, and $M^2 C_c$ is the component of force coefficient in the chord axis, positive towards trailing edge. The moment coefficient is negative for pitch down moments. In the normal force plots of Figure 14 of the rigid rotor simulations, the higher twist rotor shows a clearly increased area of negative lift on the advancing side of the rotor, while the 2/rev, 210 degree phase harmonic twist causes the advancing side tip to be loaded more than baseline. The high twist shows a small reduction in sectional pitching moment on the rear of the disk, while the 2/rev harmonic input reduces it near 100 degrees of azimuth

between 80%R and 90%R. Figure 15 shows the Mach-squared force coefficients of the elastic simulations. The rotor tip on the advancing side is generally more offloaded due to pitch down moment. The loss of lift in the outboard advancing and retreating regions is visible on the high-twist rotor. The 2/rev shows the opposite effect at these locations, as the twist is minimal at 105 and 280 degrees of azimuth. The sectional chordwise force plots are almost unchanged from the rigid simulations. The higher twisted blade showed moment coefficient reductions, mainly near 80%R at all azimuth stations except the front of the disk.

Table 7 Trim states, force coefficients, vibration index and lift-to-drag, in rigid rotor forward flight.

	rigid, baseline	rigid, twisted	rigid, 2/rev
θ_{75} [degrees]	10.60	10.20	9.50
θ_{1s} [degrees]	-0.89	-1.30	-1.10
θ_{1c} [degrees]	5.33	7.40	7.25
C_Q^{US}/σ	8.104×10^{-3}	7.788×10^{-3}	8.109×10^{-3}
C_L^{US}/σ	6.256×10^{-2}	6.111×10^{-2}	6.359×10^{-2}
C_D^{US}/σ	-1.149×10^{-2}	-1.051×10^{-2}	-1.103×10^{-2}
L/D_e	5.32	5.16	5.20
VI (eqn. 4)	0.0291	0.0872	0.0591

Table 8 Trim states, force coefficients, vibration index and lift-to-drag, in elastic rotor forward flight.

	elastic, baseline	elastic, twisted	elastic, 2/rev
θ_{75} [degrees]	11.04	10.90	10.00
θ_{1s} [degrees]	-1.23	-1.100	-1.42
θ_{1c} [degrees]	6.23	6.00	5.60
C_Q^{US}/σ	7.967×10^{-3}	7.625×10^{-3}	7.775×10^{-3}
C_L^{US}/σ	6.429×10^{-2}	6.302×10^{-2}	6.427×10^{-2}
C_D^{US}/σ	-1.100×10^{-2}	-1.016×10^{-2}	-1.104×10^{-2}
L/D_e	5.42	5.38	5.43
VI (eqn. 4)	0.1012	0.1025	0.0848

IX. Conclusion and Future Work

This paper presents hover results for model-scale blades and focuses on the effect of blade twist. The HVAB, STAR and ATR are of rather simple planforms. This helped identify the effect of increased twist which improves the figure of merit of the blades in hover. Increasing the linear twist distribution by 4 degrees over the blade radius, resulted in a 2 count improvement for the HVAB and a 3 to 4 count improvement for the STAR rotor. With the HVAB being almost twice as twisted than the STAR blade, diminishing returns at higher twist angles were expected. The ATR rotor showed a 2 count FM improvement at a 10 degree pitch setting, with the same twist increase. The benefits are mainly drawn from the changes in the blade spanwise loading induced by the twist, where higher twisted blades carried more load inboards and offloaded the tip. It is this off-loading of the tip that helped reduce the induced power, leading to an higher figure of merit. In high advance-ratio forward flight, the twist increase on the STAR rotor lead to a slightly increased vibration index and reduction in lift to drag ratio. Trends between rigid and elastic simulations could be established, with the elastic rotor simulation showing higher lift to drag ratio, but also larger vibration. A harmonic active twist could significantly reduce the vibration index in both rigid and elastic cases. This work is now directed towards investigating the effect of increased twist and harmonic input at different forward flight cases.

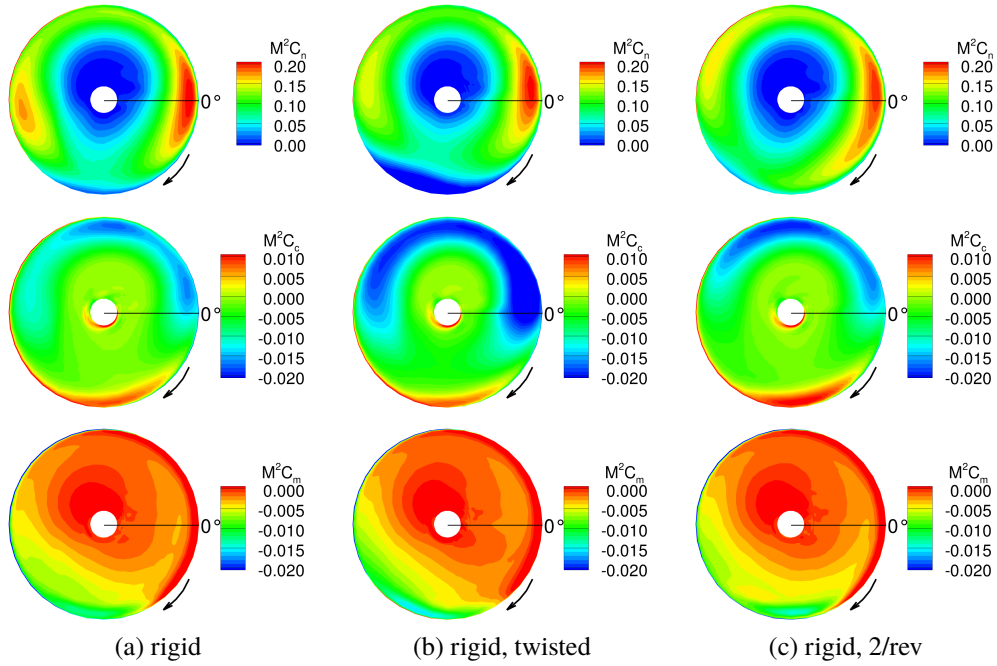


Fig. 14 Rigid STAR level flight M^2 sectional normal force, chordwise force and moment coefficients.

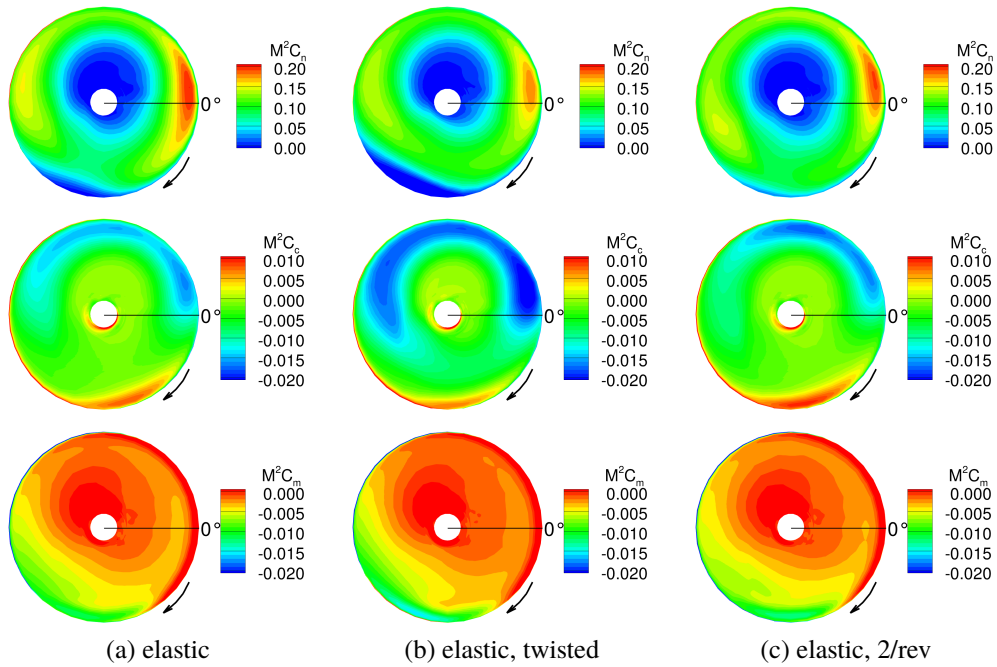


Fig. 15 Elastic STAR level flight M^2 sectional normal force, chordwise force and moment coefficients.

Acknowledgments

The financial support received by the Defence, Science and Technology Laboratory (DSTL) of UK, under contract No. DSTLX10000129255 is gratefully acknowledged. Data for the STAR rotor were kindly made available by DLR in the joint funded research project. Part of the results were obtained using the EPSRC funded ARCHIE-WeSt High Performance Computer (www.archie-west.ac.uk). EPSRC grant no. EP/K000586/1.

References

- [1] “Rotorcraft Hover Prediction Workshop (HPW),” <https://www.aaiaa-hpw.org/hvab-rotor>, 2020. Accessed: 2022-09-13.
- [2] Balch, D., and Lombardi, J., *Experimental Study of Main Rotor Tip Geometry and Tail Rotor Interactions in Hover. Volume 1. Text and Figures*, NASA-CR-177336-VOL-1, 1985.
- [3] Watkins, A. N., Leighty, B. D., Lipford, W. E., Goodman, K. Z., Crafton, J., and Gregory, J. W., “Measuring Surface Pressures on Rotor Blades Using Pressure-Sensitive Paint,” *AIAA Journal*, Vol. 54, No. 1, 2016, pp. 206–215. <https://doi.org/10.2514/1.J054191>, URL <https://doi.org/10.2514/1.J054191>.
- [4] Overmeyer, D., Copp, P., and Schaeffler, N., “Hover Validation and Acoustic Baseline Blade Set,” Tech. Rep. NASA-TM-2020-5002153, AIAA, NASA, May 2020.
- [5] Jimenez-Garcia, A., and Barakos, G. N., “Hover Performance Predictions for the S-76 Main Rotor Blade,” 2015. <https://doi.org/10.2514/6.2015-1712>.
- [6] Jimenez-Garcia, A., and Barakos, G. N., “Hover predictions of the S-76 rotor using HMB2-model to full-scale,” 2016. <https://doi.org/10.2514/6.2016-0299>.
- [7] Jimenez-Garcia, A., and Barakos, G. N., “CFD Simulations of the ERICA tiltrotor using HMB2,” 2016. <https://doi.org/10.2514/6.2016-0329>.
- [8] Jimenez-Garcia, A., Colonia, S., and Barakos, G., “Accurate predictions of hovering rotor flows using CFD,” 2017. <https://doi.org/10.2514/6.2017-1666>.
- [9] Jimenez-Garcia, A., and Barakos, G. N., *Prediction of helicopter rotor hover performance using high fidelity CFD methods*, 2017. <https://doi.org/10.2514/6.2017-3053>.
- [10] Bauknecht, A., Ewers, B., Schneider, O., and Raffel, M., “Blade tip vortex measurements on actively twisted rotor blades,” *Experiments in Fluids*, Vol. 58, No. 5, 2017.
- [11] Kalow, S., van de Kamp, B., Keimer, R., and Riemenschneider, J., “Next generation active twist helicopter rotor blade - Simulated results validated by experimental investigation,” 2019, p. 1378 – 1386.
- [12] van der Wall, B. G., Lim, J. W., Riemenschneider, J., Kalow, S., Wilke, G. A., D. Douglas, J. B., Bailly, J., Delrieux, Y., Cafarelli, I., Tanabe, Y., Sugawara, H., Jung, S. N., Hong, S. H., Kim, D.-H., Kang, H. J., Barakos, G., and Steininger, R., “Smart Twisting Active Rotor (STAR) - Pre-Test Predictions,” *48th European Rotorcraft Forum*, 2022.
- [13] Jimenez-Garcia, A., and Barakos, G., “Numerical simulations on the PSP rotor using HMB3,” 2018. <https://doi.org/10.2514/6.2018-0306>.
- [14] Fitzgibbon, T. A., Woodgate, M. A., Jimenez-Garcia, A., and Barakos, G. N., “Validation of the Steady-State Hover Formulation for Accurate Performance Predictions,” *AIAA Journal*, Vol. 57, No. 12, 2019, pp. 5293–5308. <https://doi.org/10.2514/1.J058408>, URL <https://doi.org/10.2514/1.J058408>.
- [15] Fitzgibbon, T., and Barakos, G., “Investigation of Wake Breakdown in Hover Using The HMB3 Solver,” 2022. <https://doi.org/10.2514/6.2022-1320>.
- [16] Rauch, P., Gervais, M., Cranga, P., Baud, A., Hirsch, J., Walter, A., and Beaumier, P., “Blue EdgeTM: The Design, Development and Testing of a New Blade Concept,” Virginia Beach, VA, USA, 2011.
- [17] Duque, E. P. N., “A Numerical Analysis of the British Experimental Rotor Program Blade,” Boston, MA, USA, 1989.
- [18] Steijl, R., Barakos, G. N., and Badcock, K., “A framework for CFD analysis of helicopter rotors in hover and forward flight,” *International Journal for Numerical Methods in Fluids*, Vol. 51, No. 8, 2006, pp. 819–847. DOI: 10.1002/d.1086.

- [19] Osher, S., and Chakravarthy, S., “Upwind schemes and boundary conditions with applications to Euler equations in general geometries,” *Journal of Computational Physics*, Vol. 50, No. 3, 1983, pp. 447–481. DOI: 10.1016/0021-9991(83)90106-7.
- [20] van Leer, B., “Towards the ultimate conservative difference scheme. V.A second-order sequel to Godunov’s Method,” *Journal of Computational Physics*, Vol. 32, No. 1, 1979, pp. 101–136. DOI: 10.1016/0021-9991(79)90145-1.
- [21] van Albada, G. D., van Leer, B., and Roberts, W. W., “A Comparative Study of Computational Methods in Cosmic Gas Dynamics,” *Astronomy and Astrophysics*, Vol. 108, No. 1, 1982, pp. 76–84. DOI: 10.1007/978-3-642-60543-7.
- [22] Jameson, A., “Time-Dependent Calculations Using Multigrid, with Applications to Unsteady Flows past Airfoils and Wings,” *AIAA 10th Computational Fluid Dynamics Conference*, 1991.
- [23] Axelsson, O., *Iterative Solution Methods*, Cambridge University Press: Cambridge, MA, 1994. DOI: 10.1017/CBO9780511624100.
- [24] Menter, F. R., “Two-Equation Eddy-Viscosity Turbulence Models for Engineering Applications,” *AIAA Journal*, Vol. 32, No. 8, 1994, pp. 1598–1605. DOI: 10.2514/3.12149.
- [25] Dehaeze, F., “Aeroelastic Analysis of Turbulent Rotor Flows,” Ph.D. thesis, University of Liverpool, 2012.
- [26] Shin, S., Cesnik, C. E. S., and Hall, S. R., “Closed-Loop Control Test of the NASA/Army/MIT Active Twist Rotor for Vibration Reduction,” *Journal of the American Helicopter Society*, Vol. 50, No. 2, 2005, pp. 178–194.
- [27] Kocurek, J., and Tangler, J., “A Prescribed Wake Lifting Surface Hover Performance Analysis,” *Journal of The American Helicopter Society*, Vol. 22, 1977, pp. 24–35.